Journal of Volcanology and Geothermal Research 454 (2024) 108178

Contents lists available at ScienceDirect

Journal of Volcanology and Geothermal Research

journal homepage: www.journals.elsevier.com/journal-of-volcanology-and-geothermal-research

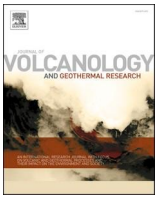

Crystal mush interaction controls eruptive style during the 2018 Kīlauea fissure eruption

Arianna Soldati [a,b,*], Daniel Weidendorfer [b], Corrado Cimarelli [b], Ulrich Kueppers [b], Bruce F. Houghton [c], Caroline M. Tisdale [c], Donald B. Dingwell [b]

[a] Department of Marine, Earth and Atmospheric Sciences, North Carolina, State University, Raleigh, NC, USA
[b] Department of Earth and Environmental Sciences, LMU Munich, Theresienstraße 41, 80333 Munich, Germany
[c] Department of Earth Sciences, University of Hawaii at Manoa, Honolulu, HI, USA

ARTICLE INFO

Keywords:
Kilauea 2018
F17
Magma mixing

ABSTRACT

We use new geochemical, petrological, and rheological data to constrain the formation and emplacement of the highly compositionally unusual(andesitic basalt) Kīlauea 2018 Fissure 17 (F17) eruptive products. Despite the restricted spatial and temporal distribution, F17 samples are texturally and geochemically diverse. The western samples are enriched in SiO_2 by up to 10 wt%, relative to their eastern equivalents; additionally, the western samples contain microcrystalline enclaves, absent from the homogenous eastern samples. The compositions erupted along F17 suggest interaction between the basaltic 2018 juvenile magma and a crystal mush at depth, likely a left-over from the nearby 1955 eruption. Magma mingling caused heating and local melting of remnant mush, leading to melt hybridization and volatile exsolution. Rapid water exsolution likely caused over-pressurization of the reservoir underneath the western side of F17, leading to Strombolian explosions of viscous magma, in contrast to sustained Hawaiian fountaining on the eastern side. Remelting of remnant crystal mush and melt hybridization in open-conduit systems may hence be an effective mechanism in inducing volatile saturation.

1. Introduction

1.1. Eruptive activity along F17 during the 2018 Kīlauea eruption

Many basaltic eruptions start along fissures, with activity rapidly localizing at discrete eruptive vents in response to thermal and rheological feedback loops (Jones and Llewellin, 2021). Notable recent examples of such activity include the 2014–2015 Holuhraun (Iceland) eruption (Pedersen et al., 2017), the 2018 Etna (Italy) eruption (Correale et al., 2024), and the 2021 Fagradasfjall (Iceland) eruption (Pedersen et al., 2022). Activity can range from sustained steady or unsteady Hawaiian fountaining to rapid and normal Strombolian explosions, as well as be purely effusive. Either way, lava flows are typically produced.

In 2018, Kīlauea had been erupting almost continuously since 1983, often along the East Rift Zone (ERZ). On May 3rd 2018 a new eruption started (note that this would more properly be identified as an episode within the 1983–2018 eruption; however, most relevant literature refers to the 2018 events as an eruption), with the first of 24 eruptive fissures opening at approximately 4:30 am Hawaiian Standard Time (HST) in the lower ERZ (LERZ). Additional fissures formed semi-randomly both up- and down- rift of their predecessors, reaching a final length of 6.8 km. The last surface discharge of magma occurred on August 4th 2018. This eruption produced approximately 1 km^3 of lava over 90 days (Neal et al., 2019), accompanied by caldera collapse at Kīlauea's summit (Anderson et al., 2019). Gansecki et al. (2019) recognized three main eruption phases of contrasting chemistry and eruptive style. We focus here on the rheology of the products of F17, the longest fissure (470 m) generated in 2018 (Houghton and Tisdale, 2022). F17 is the most down-rift of the 2018 fissures and is also displaced 200 m north of the main F11–F18 line of fissures (note that the fissures are numbered chronologically rather than spatially; Gansecki et al., 2019). Notably, F17 has the widest range of lava chemistry (Gansecki et al., 2019; Pietruszka et al., 2021) and diversity in eruptive style (Houghton et al., 2020). The more evolved compositions (andesites) are found at the western end of the fissure and the least evolved ones (basaltic andesites) at the eastern end (Gansecki

* Corresponding author at: Department of Marine, Earth and Atmospheric Sciences, North Carolina, State University, Raleigh, NC, USA.
E-mail address: a.soldati@ncsu.edu (A. Soldati).

https://doi.org/10.1016/j.jvolgeores.2024.108178
Received 17 April 2023; Received in revised form 20 August 2024; Accepted 27 August 2024
Available online 29 August 2024

et al., 2019). Eruptive dynamics spanned the unsteady Hawaiian (at the western end) to rapid Strombolian (at the eastern end) range.

Activity at F17 began at approximately 4:30 am HST on May 13th (Neal et al., 2018) and had three phases. During Phase 1 (May 13th–May 14th), the fissure had two clear parts: a ~ 300 m long line of spattering and weakly fountaining vents in the east and in the center, and a second cluster of normal Strombolian vents in the west, which collectively fed a small ʻaʻā lava flow, which drained eastwards over a gently sloping, planar surface. During Phase 2 (May 15th–20th), one eastern vent increased in vigor to form an unsteady low fountain, which reached heights of 50 to 80 m above the vent at its peak (on May 18th). At the time, it was possible to divide the fissure into three segments, A, B, and C. Segment A was centered on the eastern vent, where Hawaiian fountaining built a small, symmetrical cone. Segment B constituted the middle portion of the fissure, which contained numerous clusters of 3 to 5 closely spaced vents that showed alternating eruptive behaviour between rapid Strombolian and unsteady Hawaiian. These vents were the first to cease being active, and they were subsequently submerged by lava draining from more western sources. Segment C consisted of a chain of western vents, spaced approximately 10 m apart, showing Strombolian explosions pulsating at intervals of tens of seconds to several minutes. Explosions in B and C took place through a carapace of slowly moving lava. Finally, during phase 3 (May 21st–25th) the activity in A declined sharply and was reduced to incandescence by early May, segment B was quiet, and Strombolian explosions continued with reduced frequency and vigor in C. No activity was observed or reported from F17 after May 25th.

It is worth noting that F17 opened in a very active portion of the LERZ, which had seen at least two major eruptions in the 20th century. In 1955, a 15-km-long fissure system (Fig. 1) erupted basaltic, porphyritic lavas (Ho and Garcia, 1955; Wright and Fiske, 1971). Five years later, another fissure eruption took place nearby, erupting magmas that appeared to be genetically related to the 1955 magma, leading Murata and Richter (1966) to hypothesize that 40 million cubic meters of magma failed to erupt in 1955 and were later remobilized in 1960. Finally, in 2005, magma with dacitic melt composition was encountered during geothermal exploration of well KS-13 at the Puna Geothermal Venture at a depth of 2488 m (Teplow et al. 2009; Fig. 1).

1.2. Melt-crystal mush interaction

Volcanic rocks and their subvolcanic intrusive equivalents contain information on magma storage conditions. The chemistry of freshly erupted ocean island basalts at active shield volcanoes such as Kīlauea yields first order insights into chemical melt differentiation under subvolcanic P-T conditions (Sun and Dasgupta, 2023). During magma ascent, silicate melts physically interact and chemically re-equilibrate with host rocks through wall rock assimilation and metasomatism (Gao et al., 2022; Palummo et al., 2024; Loges et al., 2019). Thus, progressive re-equilibration between buoyancy-driven melts and surrounding wall-rocks may yield control on fluid exsolution and on triggering explosive volcanism (Weidendorfer et al., 2019; Rout and Wörner, 2020). Additionally, shallow magma reservoirs cool at higher rates at the margins than at the center, and crystals settle out or float up depending on their density contrast with the parent magma. Gutiérrez and Parada (2010) highlight how a shallow magma chamber can

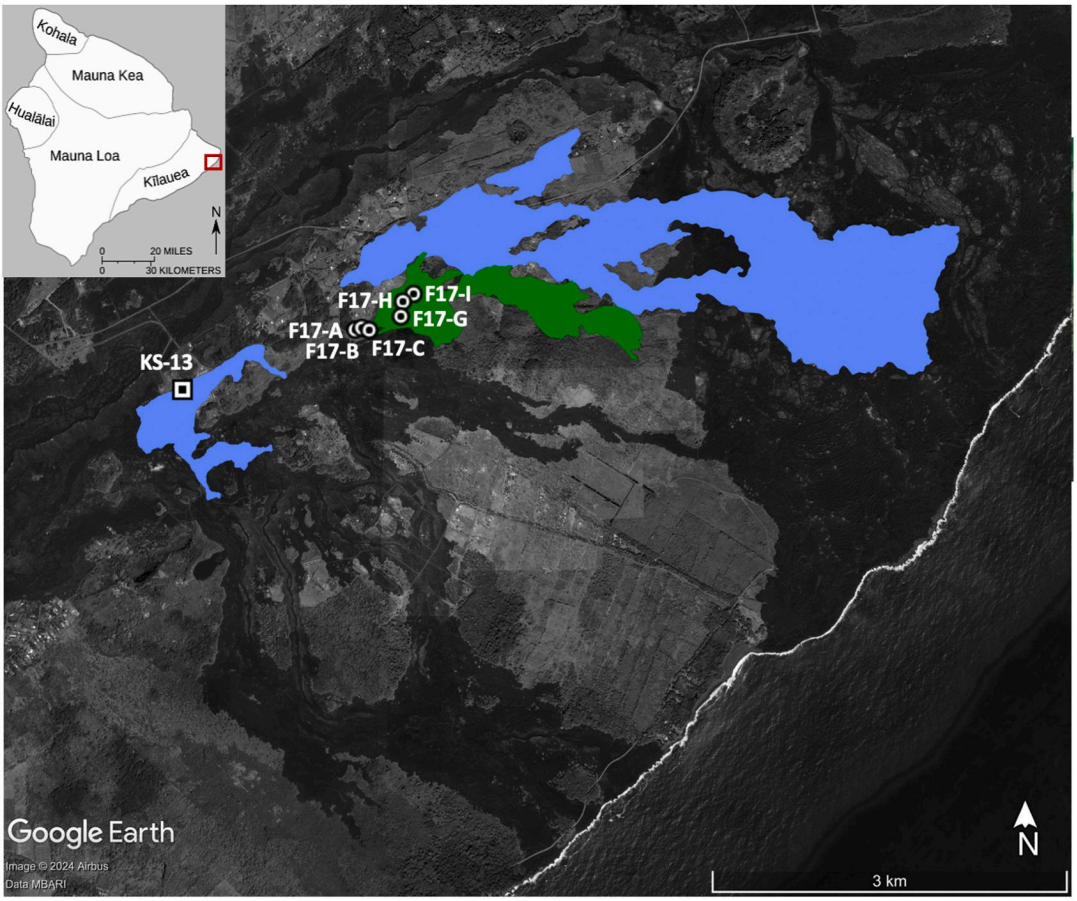

Fig. 1. Map of the F17 flow (green), highlighting sample locations (F17-A,B,C,G,H,I); the 1955 eastern flows (blue) are also shown, together with the location of well KS-13.Inset map shows location on the Big Island. (For interpretation of the references to colour in this figure legend, the reader is referred to the web version of this article.)

produce compositionally different liquids co-existing at temperature contrasts of several hundred degrees early within the reservoir's cooling history. F17 provides unique insights into fissure-fed eruptions covering a range of emplacement dynamics (steady vs. unsteady explosive and effusive activity) and spanning in chemical composition of the erupted material from basaltic andesites to andesites. Previous studies used trace elements and melt inclusion volatile content to identify the parent magma of the compositions erupted at F17, as well as identifying their storage depth (Wieser et al., 2022). This study combines geochemical and textural analyses of pyroclasts erupted along F17 with super-liquidus viscosity measurements of natural bulk rock and synthetic interstitial melt to better constrain chemical disequilibrium reactions between basaltic melts replenishing subvolcanic basaltic crystal mush beneath the LERZ of Kīlauea.

2. Materials and methods

2.1. Sample selection and preparation

Representative samples were collected along F17 between September 2018 and February 2020 after the end of the eruption, which have already been partly described by Soldati et al. (2021). In this study we focus on three sample localities at each end of fissure F17, for a total of six samples. Samples F17-A, F17-B, and F17-C were taken from the western end of the fissure (F17-West; segment C); F17-G, F17-H, and F17-I from the eastern end (F17-East; segment A). Segment B – the middle segment of Fissure 17 – is not represented in our sample suite because primary pyroclastic material from those vents were rapidly covered by lavas emitted to the West of them and it is thus not possible to sample them today.

Sample locations are reported in Table 1 and shown in Fig. 1.

Samples were mostly collected as coarse lapilli and fragments of broken small bombs (3.2 to 28 cm) from each locality and were cut, mounted in epoxy resin, polished, and carbon coated for textural and geochemical characterization.

Melt viscosity of re-melted natural whole-rock samples and of synthetic compositions replicating interstitial glasses of the F17-East and F17-West pyroclasts were performed at 1 atm and super-liquidus temperatures. Whole-rock samples were initially crushed into 1–3 mm chips, loaded in a $Pt_{80}Rh_{20}$ crucible, and subsequently melted in air at 1600 °C for at least 30 min using a box furnace. The resulting melts were then rapidly quenched by pouring them onto a cold copper disc, then crushed and re-melted again to ensure chemical homogenization.

Additionally, three starting materials for viscosity measurements were synthesized from high-purity reagent-grade oxide and carbonate powders to match the major element composition of interstitial glasses of F17-A and F17-H as well as the interstitial glass within the entrained enclaves in F17-A. After weighing the powders together, the mixtures were homogenized for 5 min in a shatter box before being fused to silicate glasses under the same conditions as the natural samples.

2.2. Analytical methods

Pyroclast textures (2D) and the mineral phase assemblage surrounded by silicate groundmass glass were characterized by scanning electron microscopy (SEM, Hitachi SU5000) at LMU Munich. Automated counting, size distribution, and further geometrical characteristics of microlites and pyroclastic void space was performed with the FIJI (v.2.1) software (Schindelin et al., 2012) using post-processed scaled back-scattered electron images. Post-processing consisted of manusally tracing the major axis of each microlite on one separate layer with an Apple pencil on an iPad in the Adobe Draw software. The average sizes of microlites within F17-West entrained enclaves was then determined using FIJI.

Groundmass silicate glasses and minerals of the natural pyroclast samples as well as the fused whole-rock and synthetic glasses were analyzed for major element chemistry by electron probe micro-analyzer (EPMA; Cameca SX100) at LMU Munich. SiO_2 and Na_2O were standardized on albite, MgO on periclase, Al_2O_3 and K_2O on orthoclase, P_2O_5 on apatite, CaO on wollastonite, FeO on ilmenite, MnO on bustamite, and Cr_2O_3 on chromite. For silicate glass analyses, an accelerating voltage of 15 kV was applied with a beam current of 10 nA and 10 μm beam spot size. Minerals were analyzed with 20 kV accelerating voltage, 10 nA beam current on a focused beam. Counting times were 10 s on the peak and the background was recorded for 5 s on each side. At least 3 spot analyses were performed for each phase. Several different crystals were analyzed for each mineral phase, and multiple analyses (3−10) were obtained for each phenocryst. Oxides and some pyroxene microlite analyses were limited due to their small size of <10 μm, thus only a few data points were collected on crystal larger than the chosen spot size.

2.3. Viscosity measurements

The melt viscosity of whole-rock samples and synthetic replicates of interstitial silicate glasses was measured at LMU Munich by concentric cylinder viscometry at super-liquidus temperatures and 1 atm using a Brookfield DVIII+ measuring head with full torque range between 0 and 0.7187 mNm. The apparatus consists of a cylindrical spindle immersed in a cylindrical crucible. The measuring crucible (h = 51 mm, r = 13.3 mm) and spindle (l = 33.2 mm, r = 7.2 mm, with 45 °conical top and bottom terminations) are made of $Pt_{80}Rh_{20}$ and were iron-saturated. The spindle is rotated at constant speed. The sample exerts a measured torque proportional to its viscosity on the rotating spindle, which is then calculated. Two calibrations are performed on this crucible-spindle pair using standard glass DGG 1 (Meerlender, 1975): a thermal calibration spanning the entire experimental temperature range and a rotation-rate-based viscometer calibration over the full range of rotation rates employed. The precision of the resulting viscosity values is ±3 % (Dingwell, 1986).

The sample is initially held at super-liquidus conditions (1531 °C) and stirred for at least three hours to ensure complete homogenization. Set temperature is then reduced stepwise in 25 °C intervals until the onset of crystallization, which is detected as a long-term increase in viscosity at constant temperature. Each temperature step consists of a one-hour dwell, which allows the sample to reach thermal equilibrium as indicated by steady-state viscosity readings. Finally, the sample is reheated to the initial temperature and its viscosity is measured again to exclude any potential instrumental or sample drift. The initial rotation speed at 1531 °C is between 40 and 1.2 rotations per minute (RPM) depending on sample viscosity, and is then automatically halved with decreasing temperature whenever the torque exceeds 100 %, down to a minimum value of 0.1 RPM.

Table 1
Sample locations reported as latitude and longitude.

		Latitude	Longitude
F17W	A	19°28′56.21″N	154°52′32.14″W
	B	19°28′56.76″N	154°52′30.11″W
	C	19°28′56.11″N	154°52′27.77″W
F17E	G	19°29′0.16″N	154°52′18.03″W
	H	19°29′4.56″N	154°52′17.46″W
	I	19°29′6.83″N	154°52′14.19″W

3. Results

3.1. Textural and petrographic characteristics

F17 pyroclasts are divided hereafter in two groups, the western (F17-West) and eastern (F17-East) eruption products. A total of six representative samples, three from the Western and three from the Eastern end of F17, were analyzed texturally and petrographically, focusing on

crystal populations. Here, phenocrysts are defined as cogenetic crystals >100 μm and microlites are defined as cogenetic crystals <100 μm.

F17-West samples consist of a host containing magmatic enclaves that range in size from 10^{-5} m to 10^{-2} m (Fig. 3). The host is microlite-rich with very few phenocrysts and xenocrysts (some of which are partially resorbed) The average phenocryst length (major axis of 2D crystals) is 170 μm. The average microlite length varies between 26 μm and 33 μm depending on sample; the median microlite length is 23–27 μm, and the mode is 16–24 μm (Table 2). About 80 % of microlites are less than 50 μm long. The microlite size distribution is positively skewed for all samples. Microlites are overwhelmingly aligned around enclaves, bubbles, and phenocrysts (Fig. 2). The host of F17-West samples contains a few mostly cm-sized bubbles.

F17-West enclaves are holocrystalline, and contain a phenocryst population (average size of 175 μm) and a dominant microlite population (average size of 10–15 μm, consistently across enclaves). Enclaves contain many small bubbles of the order of 10 μm diameter. Bubbles are typically concentrated around phenocrysts.

F17-East samples comprise a phenocryst population (average length of 119–171 μm) and a dominant microlite population (average length of 26–39 μm). Minerals tend to be euhedral. F17-East samples are significantly more vesicular than samples from F17-West. Bubbles are typically mm-sized, and widespread coalescence is observed. F17-East samples do not contain enclaves.

F17-West samples are significantly more crystalline than F17-East samples, and enclaves are significantly more crystalline than their surrounding host.

3.2. Whole-rock and interstitial glass chemistry

The same samples used for textural analysis were analyzed for major element whole-rock and interstitial glass composition. A synoptic overview of F17 geochemistry can be found in Haag et al. (2024); we here present the full dataset. According to whole-rock major element variations (Table 3), pyroclasts from F17-East (samples F17-G, F17-H, F17-I) are more mafic with 52.61–54.23 wt% SiO_2, 2.68–2.87 wt% TiO_2, 8.61–8.74 wt% CaO and have a constant molar Mg / (Mg + Fe^{tot}) (X_{Mg}) of 0.44 when compared to F17-West western pyroclasts. The western samples have 59.56–61.19 wt% SiO_2, 1.72–2.24 wt% TiO_2, 5.29–6.02 wt% CaO and range in X_{Mg} from 0.29 to 0.34 (Fig. 4). Total alkalis ($Na_2O + K_2O$) range in the eastern pyroclasts from 3.88 to 4.04 wt% and in the western samples from 5.36 to 5.68 wt%. The F17-East and the F17-West pyroclasts show only minor variations in Al_2O_3 (13.31–14.02 wt%), MnO (0.16–0.20 wt%) and P_2O_5 (0.33–0.54 wt%). Interstitial glasses of F17-East range in SiO_2 from 53.37 to 55.47 wt%, in TiO_2 from 3.15 to 3.56 wt%, in CaO from 7.08 to 8.24 wt% at comparatively constant X_{Mg} of 0.33–0.36 (Fig. 4). Highest silica contents are observed in the western interstitial glasses with up to 70.12 wt% SiO_2, while TiO_2 and CaO reach values as low as 1.08 and 1.99 wt%, respectively. A larger spread in iron and magnesium content is observed in F17-West samples resulting in ranging X_{Mg} between 0.09 and 0.16. Total alkalis of interstitial silicate glasses are lowest in the eastern samples with $Na_2O + K_2O$ of 3.23–4.31 wt%, while the western pyroclasts are more alkali-rich with up to 6.38 wt% of $Na_2O + K_2O$ (Table 4).

3.3. Mineral chemistry

Most lavas erupted along the ERZ and at the summit of Kīlauea volcano contain olivine; however, in the F17 products, olivine is absent along the fissure. Following the nomenclature of Morimoto (1988), clinopyroxenes in the F17-East and F17-West samples are augites with $Wo_{23–40}En_{57-52}Fs_{20–8}$ and low-Ca pigeonites with $Wo_{8-15}En_{50-44}Fs_{42–41}$ (Supplementary Materials 2). Clinopyroxene major elements normalized to 4 cations and 12 charges display a large compositional variation within both F17 eruption sides, as evidenced by a total range of X_{Mg} (Mg / Mg + Fe^{2+}) from 0.52 to 0.86 and 0.08–0.78 Ca p.f.u. (per formula unit) with up to 0.47 Fe^{3+} / Fe^{tot} (Fig. 5). Fe^{2+}/Fe^{3+} was calculated from stoichiometry thtough maintaining charge balance between Fe^{2+} and Fe^{3+} when normalizing to a total of four cations per formula unit (for details see Wood and Banno, 1973). Overall, clinopyroxene yield <0.03 Na p.f.u. and are characterized by <0.04 Al^{VI} p.f.u., the latter being compromised by up to 0.17 Al^{IV} p.f.u. through substitution with Ti (Fig. 5). Furthermore, tetrahedrally coordinated Al varies slightly negatively with Mg + Fe^{2+} (Fig. 5), but shows a significantly steeper slope when compared to an ideal (Mg, Fe^{2+})Si ➔ $Al^{IV}Al^{VI}$ Tschermak's substitution. Euhedral clinopyroxene of F17 samples G, H and I yield X_{Mg} between 0.72 and 0.83, while partially resorbed clinopyroxene within the enclaves entrained in the western pyroclasts range in X_{Mg} from 0.74 to 0.86 (Supplementary Materials 4). Ca and Ti range in both eruption sides of fissure F17 from 0.48 to 0.78 a.p.f.u. (atomic proportion per formula unit) and 0.02–0.05 a.p.f.u., respectively. Augitic pheno- and xenocrysts range in Al from 0.09 to 0.18 with up to 0.06 a.p.f.u. Al^{VI}, regardless of sample locality along the F17 fissure (Fig. 5).

Compared to tightly overlapping pheno−/ xeno- cryst compositions

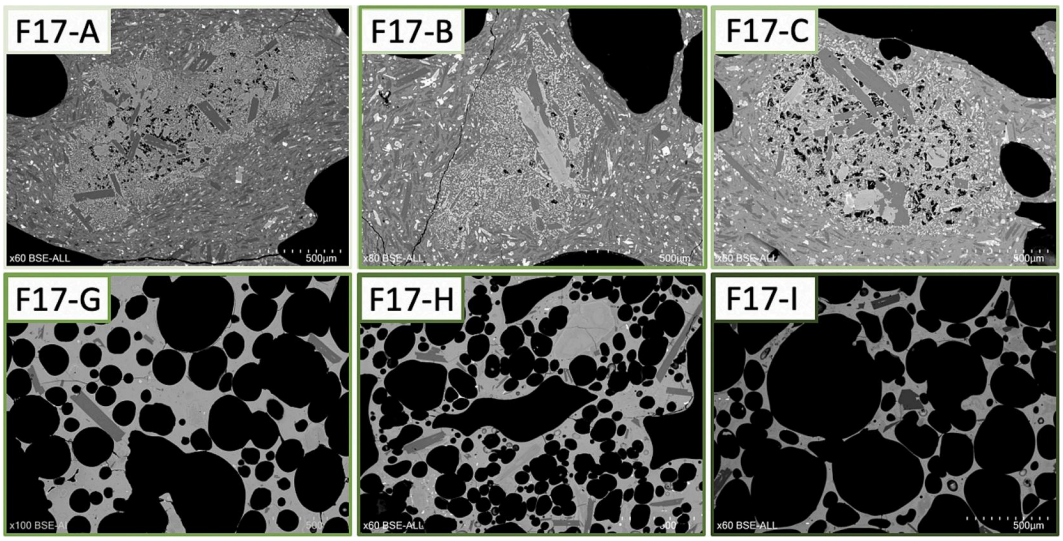

Fig. 2. Microtextures of F17 samples. Note the stark contrast between F17W samples (upper row) and F17E samples (lower row). F17W samples contain microcrystalline enclaves, absent from F17E samples. F17E samples have high vesicularity and contain abundant interstitial glass.

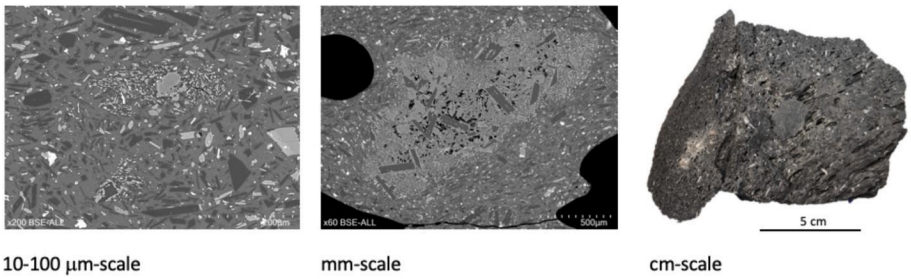

Fig. 3. Example enclave size range, from sample F17-A, spanning from µm to cm.

of the eastern and western products, clinopyroxene present as microlites in western samples (A, B and C) are subdivided into augitic compositions with 0.57–0.74 X_{Mg} and 0.55–0.78 Ca p.f.u. and low-Ca pigeonites with a more limited range in X_{Mg} of 0.52–0.56 and significantly lower Ca values between 0.18 and 0.30 a.p.f.u. (Fig. 5). No compositional difference exists between groundmass glass microlites and those crystallizing from quenched interstitial silicate melt within the enclaves (Fig. 5). Ti in microlites range from 0.01 to 0.02 a.p.f.u. in the low-Ca pigeonites to <0.07 a.p.f.u. in the augitic microlites, mirroring a coupled substitution with Al^{IV}, the latter ranging from 0.01 to 0.05 a.p.f.u. in pigeonite and 0.05–0.17 a.p.f.u. in augite microlites. Orthopyroxene is present in the eastern samples H and I (Fig. 5) with compositions near the low-Ca pigeonite to hypersthene transition in the pyroxene quadrilateral resulting in 2–3 % Wo at 75 % enstatite and 22–23 % ferrosilite components (Supplementary Materials 2). Orthopyroxene is comparatively more homogeneous with a small variation in X_{Mg} between 0.75 and 0.78 and less than 0.11 a.p.f.u. Ca. Ti and Al^{IV} range from 0.01 to 0.02 and 0.03–0.08 a.p.f.u., respectively (Fig. 5).

Feldspars range from $An_{43}Ab_{55}Or_2$ to $An_{74}Ab_{25}Or_1$ (Supplementary Materials 3). Large euhedral plagioclases enclosed by silicate glass of F17-East lavas and within F17-West enclaves overlap in An / (Ab + Or) fraction (X_{An}) between 0.58 and 0.68 (Fig. 5). The most calcic plagioclase xenocrysts within the enclaves yield X_{An} of 0.69–0.74 with a Or component between 0.002 and 0.008. Plagioclase microlites are present in F17-West lavas both in groundmass glass and within entrained enclaves (Fig. 2). These microlites have overlapping X_{An} (0.44–0.52) and $KAlSi_3O_8$ component from 0.01 to 0.02, whereas microlites from enclaves display a continuous range in Or reaching a maximum of up to 0.03 (Fig. 5). No zoning is observed in plagioclase microlites. Plagioclase phenocrysts are occasionally zoned, with the core being more calcic and the rim more sodic (Supplementary Materials 4).

3.4. Super-liquidus melt viscosities of F17 pyroclastic eruption products

Melt viscosities of lab-synthesized interstitial glasses and of whole-rock compositions are presented in Table 5. Melt viscosity is systematically higher (0.7–0.8 log units) for F17-West samples than for F17-East samples. For F17-West samples, melt viscosity increases from about 20 Pa s at 1531 °C to about 1240 Pa s at 1172 °C. For F17-East samples, viscosity increases from about 4 Pa s at 1531 °C to about 160 Pa s at 1172 °C. F17-H glass viscosity increases from 5 Pa s at 1555 °C to 139 Pa s at 1220 °C. F17-A enclave glass viscosity increases from 68 Pa s at 1555 °C to 4270 Pa s at 1220 °C, whereas F17-A host glass viscosity increases from 110 Pa s at 1555 °C to 3740 Pa s at 1267 °C.

4. Discussion

4.1. Temporal changes in MgO content of erupted Kīlauea basalts

Geophysical and petrological monitoring over the past century has proven essential to better understand Kīlauea's magmatic plumbing system and its magmatic interconnectivity between the summit vents and the kilometers-long ERZ. Based on MgO-in-glass thermometry (Helz and Thornber, 1987), lavas erupted between 1983 and 2000 had temperatures between 1180 and 1200 °C at the summit and 1150–1170 °C along the ERZ (Garcia et al., 2021). Summit lavas carried olivine, spinel, clinopyroxene, and plagioclase, while magmas void of pyroxene and feldspar were likely subject to cooling within the 18 km long ERZ dyke (Garcia et al., 2021). The experimentally determined linear relationship between temperature and basaltic glass MgO and CaO contents has widely been used to link volcanic deformation with subvolcanic recharge dynamics as well as to relate eruption activity with magma flux from tapped magma reservoirs beneath Kīlauea (e.g. Cashman and Edmonds, 2019 and references therein). In general, lavas erupted after 1983 along the ERZ are characterized by cycling MgO whole-rock concentrations ranging from 5.5 to 9.7 wt% (Thornber et al., 2015 and references therein). In comparison to relatively short-term changes of whole-rock MgO between 1983 and 2014, the corresponding matrix glasses (distance corrected after Thornber, 2001) yield considerably less variable MgO contents of 6.5–7.2 wt% MgO. Pietruszka et al. (2021) interpreted the distinctive chemistry of the MgO-rich (7.7–8.7 wt%) 2018 lavas from fissure 8 to result from mixing basalts from the summit reservoir (via Puú O'o) with differentiated ERZ magmas, the latter being stored at subvolcanic conditions since the 1960s. Based on major and trace element variations of the 2018 LERZ lavas, further assimilation of 2–6 wt% olivine would be required to explain their MgO-rich nature (Pietruszka et al., 2021).

Whole-rock analyses of F17-West lavas have 2.1–2.8 wt% MgO, which increases towards the east to 4.9–5.1 wt%. MgO in interstitial glasses is highest in samples G, H, and I, with 3.5–4.2 wt% MgO, while matrix glasses of F17-West have between 0.6 and 1.0 wt% MgO (Fig. 4; Table 4). Applying the MgO-in-basaltic glass thermometry from Helz and Thornber (1987) to the F17 products (Table 6) gives eruption temperatures between 1021 and 1032 °C for F17-West host glasses and 1019–1035 °C for the interstitial silicate glasses in the enclaves. F17-East glasses yield eruption temperatures between 1080 and 1101 °C. Please note that the error of the Helz and Thornber (1987) is ±10 °C.

Three episodes in 1983, 1997, and mid 2011 produced ERZ lavas with glass with very low MgO contents of ≤5 wt%, which were largely mimicked by corresponding whole-rock MgO concentrations (Thornber et al., 2015). The nature of these three low-MgO eruption episodes were previously interpreted to result from shallow pre-eruptive mixing of hotter and cooler magmas of similar whole-rock composition. The cooler magmas were suggested by Garcia et al. (1989, 1992) and Thornber et al. (2003) to origin from partially crystallized 1955–1977 material, which has been stored for several decades at super-solidus temperatures in shallow (< 4 km deep) magma reservoirs. Mixing of magmas with different temperatures was inferred from mineral zonation patterns, complex mineral resorption textures and from new overgrowth rims of partially resorbed olivine and pyroxene phenocrysts. Erupted lavas from the F17 fissure differ in texture and mineralogy depending on the vent locality. Well-developed euhedral plagioclase and (sub)hedral pyroxene occur in the eastern eruption sites whereas the western samples are characterized by large degrees of microlite groundmass crystallization of plagioclase and clinopyroxene. Clinopyroxene in enclaves, entrained in the western silicate groundmass glasses, is characterized by resorbed

Table 2
F17W host microlite parameters: length average, median, and mode; size distribution.

			n	average length µm	median length µm	mode length µm	0–10 µm	11–20 µm	21–30 µm	31–40 µm	41–50 µm	51–60 µm	61–70 µm	71–80 µm	81–90 µm	91–100 µm
F17-A	host	microlite	1696	26	23	18	83	560	546	267	123	57	30	12	9	9
F17-B	host	microlite	700	30	27	24	27	154	221	149	73	30	24	9	10	3
F17-C	host	microlite	651	33	27	16	17	163	190	122	57	37	22	18	15	10

crystal margins and often shows recrystallization to clinopyroxene microlites occasionally mantling nearby feldspar crystals. These resorption features of mainly the clinopyroxene in F17-West pyroclasts together with the pronounced SiO_2-enrichment of groundmass glasses is in line with magma hybridization to take place at at subvolcanic storage conditions prior to the eruption along F17.

4.2. Temperature estimates of basaltic andesite melts feeding the eruption at F17

Based on Fe-Mg exchange coefficients K_D $(Fe\text{-}Mg)^{cpx\text{-}liq}$ it turns out that none of the analyzed clinopyroxene were in chemical equilibrium with the erupted F17 groundmass glasses. Lavas erupted along the eastern side of F17 are similar in composition to the 1955 lavas (Ho and Michael, 1988). The 1955 lavas are characterized by slightly higher MgO contents of up to 0.8 wt% than the whole-rock sample F17-I and up to 1.7 wt% higher in MgO than in the interstitial glass of the same sample (Fig. 4). Modeled melt compositions in equilibrium with the observed clinopyroxene were obtained by mixing F17 pyroclast compositions with an average 1955 lava composition until the K_D $(Fe\text{-}Mg)^{cpx\text{-}liq}$ reaches 0.27 ± 0.03. In order to obtain clinopyroxene equilibrated melt compositions, ~95 % total hybridization for the F17-East samples and up to ~20 % hybridization for the F17-West samples would be required (see Supplementary Materials 5). Based on the clinopyroxene thermometer calibrated by Putirka et al. (1996), clinopyroxene within recalculated equilibrium melt compositions suggest crystallization temperatures for F17-East samples of ~1160 °C, while corrected interstitial melt compositions for F17-West samples seem to have crystallized clinopyroxene between 1050 and 975 °C. Clinopyroxene within the partially assimilated enclaves of F17-West samples yield equilibration temperatures of 1100–1020 °C (for microlites within enclaves) and ~ 1160 °C (for phenocrysts within enclaves). According to the modeled clinopyroxene crystallization temperatures it is likely that assimilated 1955 mush partially remelted, and hence, underwent melt hybridization with recharging magmas due to an overall small compositional difference between melts in the 1955 crystal mush and the intruding F17-East magma.

4.3. Crystallization sequence and mineral resorption during 2018 mafic melt recharge

Based on clinopyroxene geothermometry, F17-East samples and F17-West enclave phenocrysts yield pyroxene crystallization temperatures of ~1160 ± 30 °C. According to experimentally determined phase relationships for Bezymianny basaltic andesites (Almeev et al., 2013a), clinopyroxene crystallizes together with orthopyroxene (± plagioclase) from basaltic andesite melt ~1150 °C at bulk water contents of 1 wt% H_2O and ~ 700 MPa (Fig. 6). In case the pyroxene + plagioclase bearing basaltic melt would cool along an ascent-driven decompression path, during which, the silicate melt becomes passively enriched in H_2O. Increasing the water content in the basaltic melt likely reduces the stability fields of pyroxene and plagioclase. The clinopyroxene-in and the orthopyroxene-in are shifted at any given pressure below 500 MPa to lower temperatures when compared to the steeper plagioclase liquidus (Almeev et al., 2013a; Fig. 6). In comparison to the experimentally derived phase equilibria by Almeev et al. (2013a, 2013b) for Bezymianny basaltic andesites, the observed resorption textures of F17-East pyroxene cores (Fig. 2) could be explained by leaving between 650 and 100 MPa the clinopyroxene stability field. F17-East basaltic andesite products are characterized by (sub)hedral clinopyroxene and euhedral plagioclase coexisting with a small fraction of magnetite, which would require according to the experimental findings of Almeev et al. (2013a, 2013b) melt water contents of ≤2.5 wt% H_2O at a depth ≤ 100 MPa and temperatures ~1050–1080 °C (Fig. 6). This is in agreement with the estimated eruption temperatures for F17-East lavas of 1080–1100 ± 10 °C according to the MgO-in-basaltic-glass thermometry by Helz and

Table 3
Post-experimental EPMA major element analyses of bulk glass. Method details, including standards, are reported in section 2.2.

	SiO_2	TiO_2	Al_2O_3	FeO	MgO	MnO	Na_2O	K_2O	CaO	P_2O5	Cr_2O_3	*Total*
F17-A	60.20	1.72	14.02	9.26	2.09	0.17	4.01	1.68	5.42	0.53	0.01	*99.10*
F17-B	61.19	1.73	13.63	9.21	2.15	0.20	3.72	1.75	5.29	0.54	0.03	*99.45*
F17-C	59.56	2.24	13.39	9.71	2.79	0.16	3.76	1.60	6.02	0.43	0.02	*99.69*
F17-G	54.23	2.79	13.31	10.99	4.92	0.17	3.00	0.97	8.70	0.40	0.02	*99.50*
F17-H	53.28	2.68	13.44	11.00	4.92	0.17	3.10	0.93	8.61	0.33	0.02	*98.48*
F17-I	52.61	2.87	13.41	11.50	5.05	0.18	2.98	0.90	8.74	0.39	0.02	*98.64*

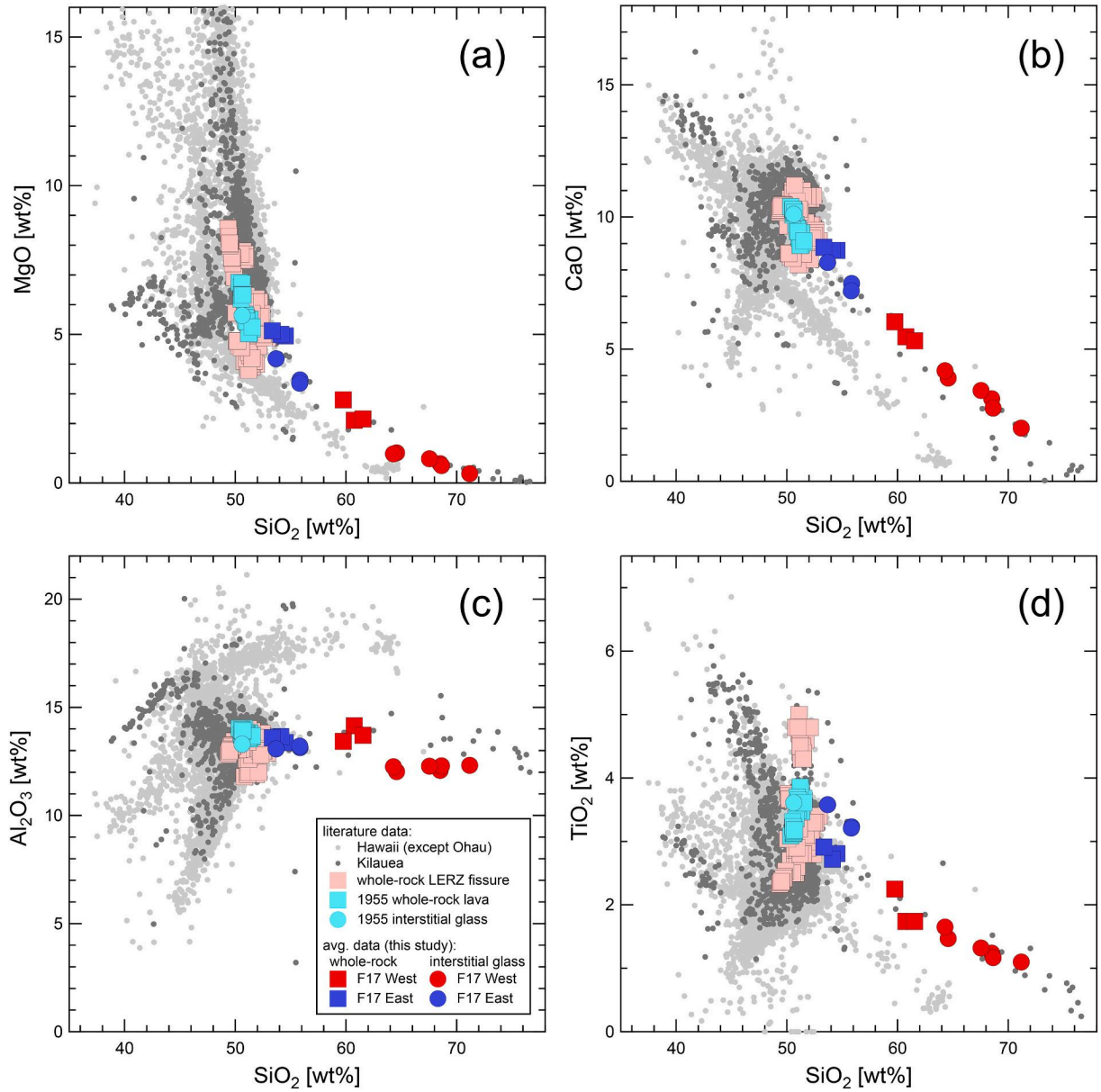

Fig. 4. Selected whole-rock glass geochemistry Harker diagrams comparing F17W and F17E samples to literature data on Kilauea (including the 1955 eruption) and Hawaii. Data represented by grey symbols are from the GEOROC database, whole-rock compositions representing the LERZ fissure from Soldati et al. (2021) Macdonald and Eaton (1964), Wright and Fiske (1971), Wright (1971) and Pietruszka et al. (2021); 1955 intersitial glass from Helz and Wright (1992).

Thornber (1987). In fact, the temperature off-set (ΔT = 30–50 °C) between the estimated eruption temperatures based on MgO-in-glass and the subvolcanic temperature at a pressure of 100 MPa, the latter inferred from phase equilibria experiments by Almeev et al. (2013a, 2013b), is likely a result of the absence of olivine in the F17 pyroclasts. The MgO-in-basaltic-glass thermometry from Helz and Thornber (1987), calibrated for Kīlauea Iki lava lake basalts at 1 atm and an oxygen fugacity (fO_2) near the nickel – nickel-oxide (NNO) buffer, is primarily used to track temporal variations of lava eruption temperatures. F17- I and -H contain plagioclase + clinopyroxene + orthopyroxene + magnetite, while F17-G pyroclasts are void of orthopyroxene and olivine. In natural basaltic andesites, olivine occurs at relatively low

Table 4
Major element analyses of natural samples interstitial glass, obtained by EPMA. Method details, including standards, are reported in section 2.2.

		SiO_2	TiO_2	Al_2O_3	FeO	MgO	MnO	Na_2O	K_2O	CaO	P_2O_5	Cr_2O_3	*Total*
F17-A	**enclave**	64.26	1.46	11.97	9.50	1.01	0.21	3.32	2.72	3.89	0.98	0.01	*99.35*
F17-B	**enclave**	70.12	1.08	12.14	5.86	0.32	0.11	3.29	3.18	1.99	0.29	0.00	*98.37*
F17-C	**enclave**	63.30	1.63	12.08	9.58	0.96	0.16	2.96	2.46	4.13	1.05	0.00	*98.31*
F17-A	**host**	68.82	1.25	12.15	7.64	0.65	0.12	3.55	2.73	3.15	0.33	0.00	*100.39*
F17-B	**host**	67.78	1.16	12.15	7.47	0.58	0.15	3.59	2.79	2.74	0.30	0.00	*98.70*
F17-C	**host**	67.10	1.31	12.20	7.66	0.81	0.13	3.63	2.56	3.42	0.49	0.02	*99.34*
F17-G		55.47	3.21	13.05	12.12	3.44	0.16	2.76	1.19	7.44	0.42	0.01	*99.28*
F17-H		54.78	3.15	12.96	11.91	3.30	0.11	3.05	1.26	7.08	0.43	0.03	*98.06*
F17-I		53.37	3.56	13.00	13.02	4.16	0.17	2.26	0.98	8.24	0.56	0.02	*99.33*

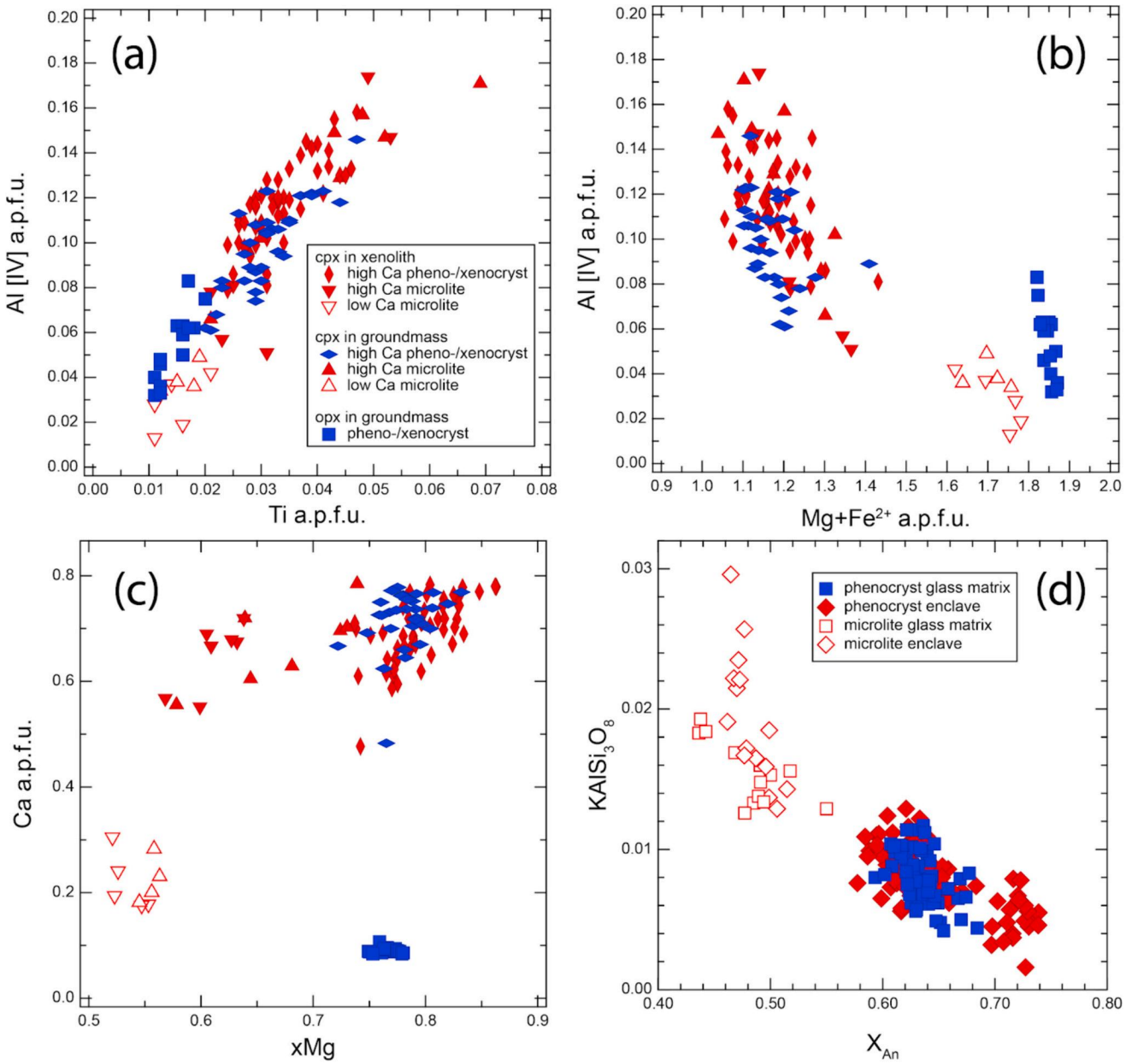

Fig. 5. Mineral chemistry of (a-c) reported clino- and orthopyroxene compositions as well as (d) feldspar pheno- and microlites.

abundance (Almeev et al., 2013a), and may even be absent due to the reaction between olivine and silicate-rich melt to form orthopyroxene (Bowen and Andersen, 1914), hence, suggesting a line of near-liquidus magma evolution close to the olivine-orthopyroxene reaction boundary. Alternatively, supercooling of basaltic melts may delay olivine nucleation, which has experimentally been shown by Donaldson (1979) to be a function of cooling rate, melt composition and the amount of initial superheating (in respect to the liquidus). Appearance temperatures of augite and pigeonite are sensitive to cooling rate and melt H_2O content. With decreasing cooling rate, the appearance temperature of

Table 5
Bulk liquid viscosities for all samples at each experimental temperature; interstitial glass viscosities of a F17 W (both host and enclave) and a F17 E sample at each experimental temperature.

T (°C)	η (Pa s)								
	F17-A	F17-B	F17-C	F17-G	F17-H	F17-I	F17-A host gl	F17-A encl gl	F17-H gl
							110	68.0	5.0
1531	20.4	20.6	15.9	3.66	4.17	3.42	141	86.4	6.0
1507	24.9	25.1	19.6	4.33	4.78	4.02	181	109	7.1
1483	30.6	31.0	24.2	5.18	5.71	4.78	234	140	8.5
1459	38.3	38.8	30.3	6.23	6.93	5.77	305	181	10.3
1435	48.5	48.9	38.1	7.62	8.40	7.02	404	237	12.7
1411	61.8	62.3	48.7	9.37	10.4	8.80	539	313	15.7
1387	80.2	80.4	62.7	11.6	13.0	10.9	727	417	19.7
1363	104	104	81.4	14.6	16.3	13.7	984	560	25.0
1339	136	137	107	18.5	20.7	17.3	1355	765	32.1
1315	182	181	141	23.8	26.9	22.3	1878	1049	41.8
1291	245	244	190	31.2	35.2	29.0	2623	1463	55.1
1267	330	331	258	41.3	46.8	38.5	3738	2064	74.1
1244	456	457	355	55.8	63.7	52.0		2937	101
1220	638	642	500	76.6	88.3	71.8		4269	139
1196	907	917	712	108	125	101			
1172	1329	1348	1037	154	179	145			
1148	1972	1999	1557		266	215			
1124	3005								

Table 6
Glass geothermometry temperatures based on the Helz and Thornber (1987) glass MgO geothermometer.

		average T (°C)
17-A	**enclave**	1034
17-B	**enclave**	1020
17-C	**enclave**	1034
17-D	**enclave**	1018
17-E	**enclave**	1027
17 -A	**matrix**	1027
17-B	**matrix**	1026
17-C	**matrix**	1030
17-D	**matrix**	1017
17-E	**matrix**	1022
17-F		1056
17-G		1084
17-H		1082
17-I		1098

augite increases. Baker and Grove (1985) showed how the peritectic reaction of olivine + liquid to pigeonite depends on volatile content in the basaltic andesite melt as well as on the cooling rate along non-equilibrium differentiation pathways. They suggest that such kinetic effects may become significant during lava flow emplacement or during magma flow through dikes or volcanic conduits. Samples from F17-East are significantly more vesicular than samples from F17-West. Bubbles are large and coalescence is observed. The pronounced vesicularity of F17-East samples (Fig. 2) is interpreted to result from *syn*-eruptive decompression vesiculation with cooling rates of the ascending conduit magma exceeding the olivine nucleation rate and a continued reaction between olivine and the melt to form low-Ca pigeonite. F17-East lavas erupt at temperatures of 1050–1100 °C, which may likely be below the olivine crystallization window of hydrous basaltic andesites in the temperature – H_2O space shown by Almeev et al. (2013b). Suppressing olivine crystallization due to supercooling would keep the MgO melt content high. The obtained eruption temperatures for the F17 products from the MgO-in-basaltic glass thermometry by Helz and Thornber (1987) would therefore appear slightly overestimated.

On the western side of fissure F17, pyroclasts carry large euhedral plagioclase, anhedral clinopyroxene and abundant magnetite as well as plagioclase microlites within a dacitic glass. This phase assemblage is explained by interaction of two magmas, 1) 2018 juvenile, 1050–1100 °C hot, basaltic andesitic magma and 2) a subvolcanic crystal mush below 100 MPa (Fig. 6), the latter which is subject to melt hybridization. The lower clinopyroxene equilibration temperature estimates (after Putirka et al., 1996) of microlites in F17-West enclaves (1020 ± 30 °C) and the upper temperature limit of microlite crystallization in F17-West matrix glasses (1060 ± 30 °C) suggest that the intruding basaltic andesite magma was likely cooled by ~40 °C (red melt evolution path in Fig. 6). Hybridization between the 2018 magma and a subvolcanic crystal mush, residing since perhaps the 1955 eruption, is texturally supported by the absence of quench features at the enclave–matrix melt interface (e.g., no chilled margins observed) in the enclave-bearing F17-West samples as well as by the continuous growth of plagioclase microlite crystals across this interface (Fig. 2). The compositional similarity and limited temperature difference between the 2018 magma and the entrained 1955 mush would allow effective melt-melt mixing resulting in hybridized andesitic magma compositions (Fig. 4). The process here described shares some similarities with the case study of the Masaya Triple Layer eruption, described by Bamber et al. (2022). Those samples also contain enclaves compositionally similar to the matrix, and are through to have crystallized from a genetically related melt that simpley cooled and crystallized longer than the matrix (Bamber et al., 2022).

4.4. *Effect of hybridization induced fluid release on the 2018 eruption dynamics*

At time of the 2018 magma intrusion, the residing 1955 crystal mush was presumably poor in magmatic volatiles. Subsequent interaction between infiltrating hydrous basaltic andesite melts and interstitial melts of the remnant mush may have resulted in hybrid melt compositions. These hybrid melts would be dacitic and yield a lower H_2O solubility than the hydrous basaltic andesite that according to experimental phase equilibria data on basaltic andesites (Almeev et al., 2013b) can contains up to 2–2.5 wt% H_2O. The drop in water solubility results in abrupt exsolution of magmatic water (Myers et al., 2014) to form an excess vapor phase at constant temperature (i.e. second boiling), which in turn increases the plagioclase stability field and hence causes plagioclase microlite crystallization within the feldspar-undersaturated silicate melt (Fig. 6). Dissolution experiments by Weidendorfer et al. (2019) have demonstrated that melt–crystal mush interaction may cause peritectic breakdown of FeMg-silicate minerals while releasing vast quantities of insoluble COH-fluid from the hybridized magma. We suggest that such sudden fluid exsolution from silicate melts at near-surface storage conditions caused volumetric stress following bubble exsolution

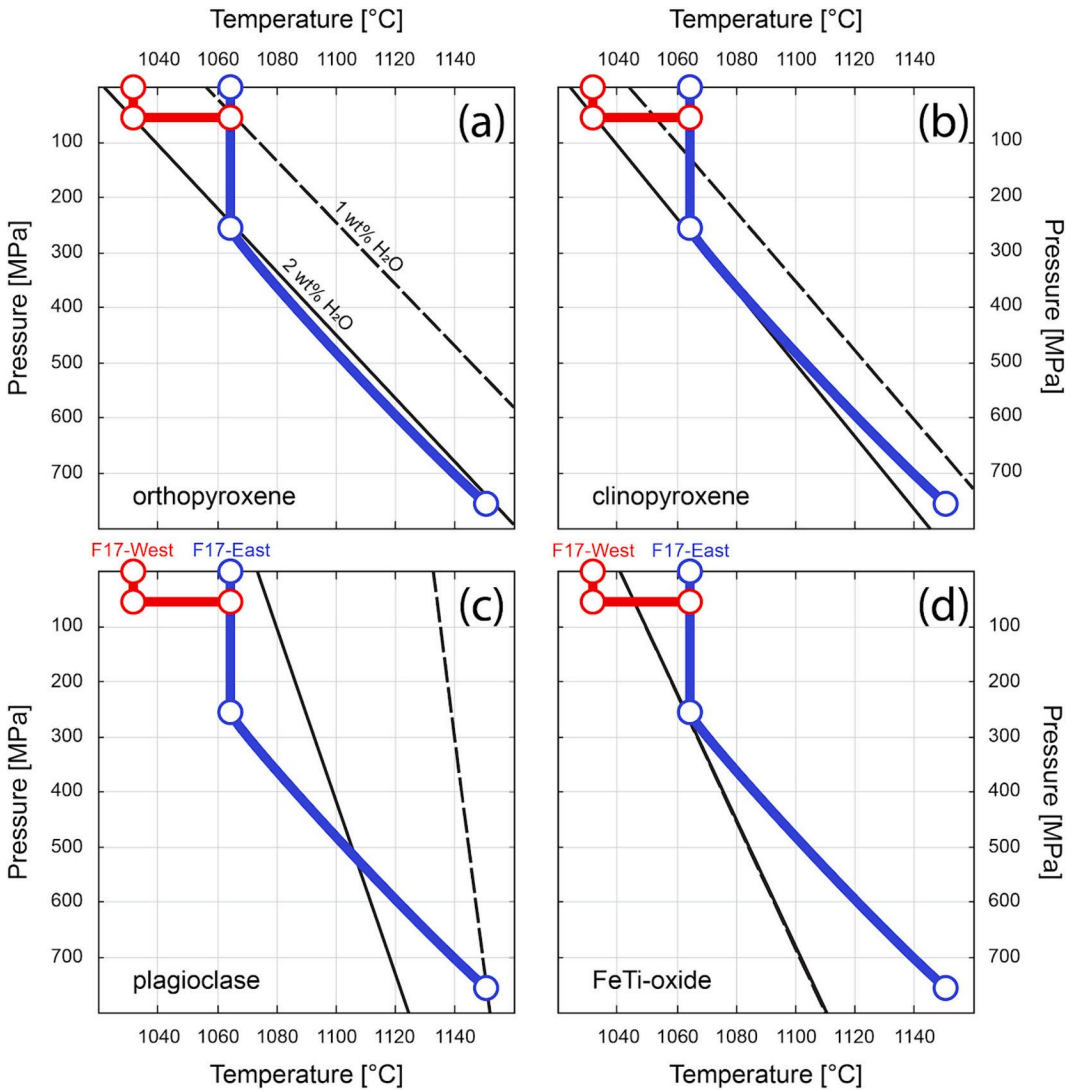

Fig. 6. Hypothesized magmatic P-T paths for the erupted F17-East (blue line) and F17-West (red line) lavas. (a-d) Black dashed and solid lines represent the orthopyroxene, clinopyroxene, plagioclase and FeTi-oxide crystallization temperatures for a basaltic andesite (Almeev et al., 2013a) at bulk water contents of 1 and 2 wt%, respectively. (a-c) According to the experimentally determined phase relationships of Bezymianny basaltic andesites (Almeev et al., 2013b), clinopyroxene crystallizes together with orthopyroxene (± plagioclase) from basaltic andesite melt ~1150 °C at bulk water contents of 1 wt% H2O and ~700 MPa. The observed resorption textures of F17-East pyroxene cores may be explained by the magma leaving the clinopyroxene stability field at pressure between 100-300 MPa. During final ascend-driven decompression along the west-side of fissure F17, the basaltic magma is being cooled by subvolcanic mush interaction, which pushes the magma into the FeTi-oxide stability field. The cooling induced crystallization of FeTi-oxides and the vast crystallization of plagioclase passively increases the F17-West magma in silica and explains the compositional offset to the F17-East lavas.

and may have contributed to triggering more violent explosive activity along the west side of F17 when compared to its eastern counterpart. Almeev et al. (2013b) showed that with decreasing P-T conditions the clinopyroxene-in and the orthopyroxene-in lines merge at bulk water contents >1 wt% and eventually may even cross each other at pressures below 100 MPa with clinopyroxene being on the high temperature side (Fig. 6b). The plagioclase – melt hygrometer from Waters and Lange (2015) gives 0.5–0.8 wt% for plagioclase microlites in the F17-West samples coexisting with clinopyroxene and magnetite as subliquidus phases. Thus, the hybridized dacitic melts erupted on the western end of F17 have likely exsolved up to 2 wt% of excess fluid during plagioclase microlite crystallization and melt hybridization at subvolcanic depth.

This sequence of events pre-dates the opening of F17 at the surface. Therefore, despite active eruption and degassing occurring simultaneously at the summit and LERZ along the main fissure system (e.g. Neal et al., 2019), locally this was still a closed system, from which the exsolved volatiles could not have escaped unhindered. Once F17 opened, the surface expression of exsolved gas accumulation was a series of discrete strombolian explosions, each driven by closely time-clustered bursting of multiple bubbles (Walker et al., 2023).

4.5. *Silica enrichment as a consequence of subvolcanic melt – Crystal mush interaction*

Silica-rich whole-rock- and interstitial glass compositions from Hawaiian shield and post-shield volcanics range in SiO_2 from 55 to 77 wt% (Fig. 4). Such silica rich volcanics were previously reported from eruptive centers including Kīlauea, Mauna Kea, Mauna Loa, Hualālai, and Kohala on Hawaii as well as at the western eruptive centers of Maui and Haleakala, and on the east-side of Molokai (Schmidt and Weidendorfer, 2018). Whole-rock and volcanic glass compositions of these eruptive centers display a negative correlation between CaO and SiO_2, (Fig. 4). This negative correlation is observed above 52 wt% SiO_2 and is also observed in the silica-rich whole-rock and in the interstitial glass

compositions of the 2018 Kīlauea lavas but at higher CaO contents for any given SiO_2 (Fig. 4). Crocket (2000) presented high silica whole-rock compositions from the Kīlauea and Mauna Ulu craters with 67.8–78.5 wt % SiO_2 and showed that hydrothermal alteration of basalts by silica-rich bearing fluids can cause such elevated silica contents. Greaney et al. (2017) reported on differentiated residual melts of the Kīlauea Iki lava lake with <6 wt% MgO and up to 57 wt% SiO_2. Such evolved ferrodiabasic compositions were interpreted by Greaney et al. (2017) to represent residual melts that have segregated from a crystal mush within the cooling lava lake. Interstitial glasses of the Kīlauea Iki segregation veins yield high silica contents of 56–74 wt% SiO_2 and low MgO concentrations ranging between 0.2 and 3 wt% (Greaney et al., 2017). In comparison, the whole-rock compositions of F17 West samples are chemically distinct from those samples on the east end of fissure F17 (Fig. 4). Both groups clearly differ in SiO_2, MgO, CaO, and $Na_2O + K_2O$ whole-rock concentrations, however, within each group the major element whole-rock chemistry displays only minor internal variation. Whole-rock samples A, B, and C are characterized by at least 5.2 wt% higher SiO_2 and 1.3 wt% higher total alkali contents when compared to the eastern samples, the latter being more enriched in MgO and CaO of at least 2.2 wt% and 2.7 wt%, respectively (Fig. 4).

The silica gap of 5–10 wt% SiO_2 between the samples from the East and the West sides of F17 is interpreted to result from hybridization-induced cooling of the western magma to temperatures below 1050 °C, where magnetite starts crystallizing under oxidizing conditions in basaltic andesites (Fig. 6; Feig et al., 2006; Almeev et al., 2013b). Recalculating major elements of interstitial silicate glasses back to their corresponding whole-rock compositions suggest total crystallinities of 21–29 % for the eastern samples with cumulate mineral proportions ranging from 0.44 plagioclase +0.56 augite to 0.48 plagioclase +0.32 augite +0.21 pigeonite. Mass-balancing the compositional offset between interstitial glasses and whole-rock of the western samples requires 52–66 % crystal accumulation in the range of 0.57 plagioclase +0.2 augite +0.13 pigeonite +0.10 FeTi-oxide to 0.59 plagioclase +0.15 augite +0.19 pigeonite +0.07 FeTi-oxide. A significantly higher FeTi-oxide abundance in the West than in the East of F17 strongly supports our hypothesis that as soon as the hybridized magma cools below the magnetite-in temperature the interstitially mixed melt is shifted from initially 54–56 wt% SiO_2 in the east to silica concentrations exceeding 60 wt% SiO_2 (Fig. 4; Fig. 6).

4.6. *Viscosity effects on magma dynamics and eruptive style*

Bulk viscosity values of remelted eruption products represent lower bounds on the erupted products viscosity, as they do not account for the effect of crystals or bubbles. Melt-only viscosity values directly represent interstitial melt viscosity. Those values are also expected to be lower than the overall magma viscosity, as they do not take into account additional phases either. However, they can inform us directly on the ability of magmas to interact with each other as they come into contact. All calculated values are anhydrous, as high temperature hydrous viscosity measurements are not possible. The magmas here considered do however contain 2–2.5 wt% water. Modelling the effect of such an amount of water on the relevant magmatic compositions throught the GRD model (Giordano et al., 2008) point to a 2-order of magnitude reducation in viscosity compared to the measured dry values. It is important to note that this variation is uniform across the relevant compositional and thermal range, and thus the viscosity ratio between the interacting magmas does not change.

F17-East bulk and interstitial melt viscosity values are typical of basaltic products, and consistent with unsteady Hawaiian fountaining style observed (e.g. La Spina et al., 2021). Since these magmas were erupted directly, i.e. without evidence of having interacted with any other magmas prior to their emplacement, no further considerations are made based on their viscosity.

The more evolved F17-West compositions have a higher melt viscosity, of the order of 10^3 Pa s at magmatic temperatures, compared to 10^2 Pa s for F17-East (consistent with the rapid and normal Strombolian eruptive styles observed at that end of the fissure; Parfitt and Wilson, 1995, Walker et al., 2023). The difference in viscosity between F17-West host and enclave melts exceeds an order of magnitude at magmatic temperature. Textural observations suggest that at the time of interaction the host melt was fluid enough for crystals to re-orient around the enclaves. However, due to the order-of-magnitude viscosity contrast, the two magmas, despite being chemically quite similar, remained physically distinct from each other, preserving the enclaves (Fig. 7).

Ho and Garcia (1955) report that the 1955 lava contained microlites and phenocrysts of olivine. Yet, we find none in any of our F17 samples, including the western ones, where we infer interaction between the juvenile magma and residing 1955 crystal mush. We note that Wieser et al. (2022) report data on one melt inclusion found in a single olivine from F17 (collected near sample F17-A from this study); additionally, up to 5 vol% olivine may have been present in their sample (Wieser, personal communication). The presence of this olivine, which may have been heterogeneously re-mobilized during magma interaction, supports a melt reaction interpretation.

Additionally, our viscosity data is consistent with most of the olivine originally present in the 1955 lava simply having settled out. Using DensityX (Iacovino and Till, 2019) we obtain a 1955 melt density value of 2550 kg/m^3 at 1100°C and 500 bars. Olivine crystals of 1 mm in diameter, having a density of 3300 kg/m^3, are thus expected to settle assuming Stokes law at a speed of $3.14 \bullet 10^{-7}$ m/s, which results in over 600 m of settling within the lifetime of the 1955 reservoir preceeding the 2018 eruption. We note that this is an end-member scenario in which olivine is the only crystallized phase. In the case of a more complex crystal mush, the viscosity of the phase through which olivine settles would be higher, resulting in lower settling velocities and ultimately less settling over the lifetime of the reservoir.

5. Conclusions

We presented novel geochemical, petrological, and rheological data on samples erupted at F17 of the the 2018 Kīlauea eruption in the Lower East Rift Zone. There is a striking 5–10 SiO_2 wt% gap in the interstitial glass phase between the samples erupted from the eastern and the western sides of the 470 m long fissure. We interpret that gap to originate from the hybridization-induced cooling of the western magma to temperatures below 1050 °C, where magnetite starts crystallizing under oxidizing conditions. Additionally, initial high water contents (up to 2–2.5 wt%) in ascending 2018 juvenile magma melts effectively suppressed plagioclase nucleation; therefore, at time of crystal mush assimilation and interstitial melt hybridization at subvolcanic (<100 MPa) P-T conditions, the resultant hybrid magma became strongly undersaturated in plagioclase. Only during the final ascent to the surface, H_2O exsolution from this hybridisised magma triggered abundant crystallization of plagioclase microlites. In the newly formed dacitic to andesitic melt, textural characteristics impeded melt-gas bubble separation enough to cause overpressurization of the magma ascending below the western side of F17, eventually resulting in explosive eruptions. Formation of an excess vapor phase in the crystal mush resulted in bubble nucleation and growth and hence mechanical decoupling of the gas phase. Eventually, this resulted in a Strombolian eruption style, in contrast with the Hawaiian fountaining observed on the eastern side of the fissure.

CRediT authorship contribution statement

Arianna Soldati: Writing – review & editing, Writing – original draft, Visualization, Supervision, Resources, Project administration, Methodology, Investigation, Funding acquisition, Formal analysis, Data curation, Conceptualization. **Daniel Weidendorfer:** Writing – review &

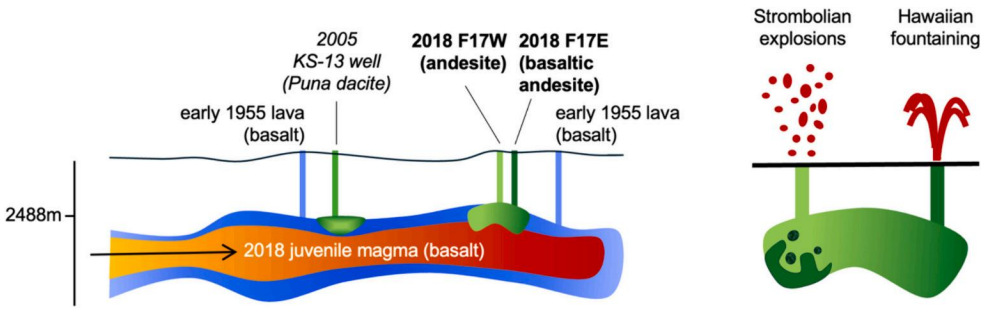

Fig. 7. Conceptual sketch of F17. Left: broader context of the area, showing the 1955 magma intrusion and surface emplacement (blue), the residual, evolved dacite tapped in 2005 at Puna (green, left), the 2018 juvenile magma (red), and the 2018 F17 compositions (green, right). Right: zoom in on F17. At the western end F17 magmas contained enclaves and were emplaced through strombolian explosions. At the eastern end they were homogenous and were emplaced through Hawaiian fountaining. (For interpretation of the references to colour in this figure legend, the reader is referred to the web version of this article.)

editing, Visualization, Methodology, Investigation, Formal analysis, Data curation, Conceptualization. **Corrado Cimarelli:** Writing – review & editing, Resources, Methodology, Investigation. **Ulrich Kueppers:** Writing – review & editing. **Bruce F. Houghton:** Writing – review & editing, Project administration, Methodology, Investigation, Funding acquisition, Conceptualization. **Caroline M. Tisdale:** Writing – review & editing, Investigation. **Donald B. Dingwell:** Writing – review & editing, Resources.

Declaration of competing interest

The authors declare that they have no known competing financial interests or personal relationships that could have appeared to influence the work reported in this paper.

Acknowledgements

A.S. C.T. and B.H. wish to acknowledge the support provided by NSF grant EAR-2119973. D.B.D. acknowledges the support of ERC 2018 AdG 834225 (EAVESDROP).

Appendix A. Supplementary data

Supplementary data to this article can be found online at https://doi.org/10.1016/j.jvolgeores.2024.108178.

References

Almeev, R.R., Kimura, J.I., Ariskin, A.A., Ozerov, A.Y., 2013a. Decoding crystal fractionation in calc-alkaline magmas from the Bezymianny Volcano (Kamchatka, Russia) using mineral and bulk rock compositions. J. Volcanol. Geotherm. Res. 263, 141–171.

Almeev, R.R., Holtz, F., Ariskin, A.A., Kimura, J.I., 2013b. Storage conditions of Bezymianny Volcano parental magmas: results of phase equilibria experiments at 100 and 700 MPa. Contrib. Mineral. Petrol. 166 (5), 1389–1414.

Anderson, K.R., Johanson, I.A., Patrick, M.R., Gu, M., Segall, P., Poland, M.P., Miklius, A., 2019. Magma reservoir failure and the onset of caldera collapse at Kīlauea Volcano in 2018. Science 366 (6470), eaaz1822.

Baker, M.B., Grove, T.L., 1985. Kinetic controls on pyroxene nucleation and metastable liquid lines of descent in a basaltic andesite. Am. Mineral. 70 (3–4), 279–287.

Bamber, E.C., La Spina, G., Arzilli, F., de'Michieli Vitturi, M., Polacci, M., Hartley, M.E., Petrelli, M., Fellowes, J. and Burton, M., 2022. Basaltic Plinian eruptions at Las Sierras-Masaya volcano driven by cool storage of crystal-rich magmas. Commun. Earth & Environ. 3 (1), 253.

Bowen, N.L., Andersen, O., 1914. The binary system MgO-SiO 2. American Journal of Science 37 (222), 487–500.

Cashman, K.V., Edmonds, M., 2019. Mafic glass compositions. Philosoph. Transac.: Math., Phys. Eng. Sci. 377 (2139), 1–24.

Correale, A., Corsaro, R.A., Miraglia, L., Paonita, A., Rotolo, S.G., 2024. The December 2018 eruption at Etna volcano: a geochemical study on melt and fluid inclusions. Frontiers in Earth Science 11, 1122132.

Crocket, J.H., 2000. PGE in fresh basalt, hydrothermal alteration products, and volcanic incrustations of Kilauea volcano, Hawaii. Geochimica et Cosmochimica Acta 64 (10), 1791–1807.

Dingwell, D.B., 1986. Viscosity-temperature relationships in the system Na2Si2O5-Na4Al2O5. Geochim. Cosmochim. Acta 50 (6), 1261–1265.

Donaldson, C.H., 1979. An experimental investigation of the delay in nucleation of olivine in mafic magmas. Contrib. Mineral. Petrol. 69 (1), 21–32.

Feig, S.T., Koepke, J., Snow, J.E., 2006. Effect of water on tholeiitic basalt phase equilibria: an experimental study under oxidizing conditions. Contrib. Mineral. Petrol. 152 (5), 611–638.

Gansecki, C., Lee, R.L., Shea, T., Lundblad, S.P., Hon, K., Parcheta, C., 2019. The tangled tale of Kīlauea's 2018 eruption as told by geochemical monitoring. Science 366 (6470), eaaz0147.

Garcia, M.O., Ho, R.A., Rhodes, J.M., Wolfe, E.W., 1989. Petrologic constraints on rift-zone processes. Bull. Volcanol. 52 (2), 81–96.

Garcia, M.O., Rhodes, J.M., Wolfe, E.W., Ulrich, G.E., Ho, R.A., 1992. Petrology of lavas from episodes 2–47 of the Puu Oo eruption of Kilauea Volcano, Hawaii: evaluation of magmatic processes. Bull. Volcanol. 55 (1), 1–16.

Garcia, M.O., Pietruszka, A.J., Norman, M.D., Rhodes, J.M., 2021. Kīlauea's Pu 'u 'Ō 'ō Eruption (1983–2018): a synthesis of magmatic processes during a prolonged basaltic event. Chem. Geol. 581, 120391.

Giordano, D., Russell, J.K., Dingwell, D.B., 2008. Viscosity of magmatic liquids: a model. Earth and Planetary Science Letters 271 (1–4), 123–134.

Greaney, A.T., Rudnick, R.L., Helz, R.T., Gaschnig, R.M., Piccoli, P.M., Ash, R.D., 2017. The behavior of chalcophile elements during magmatic differentiation as observed in Kīlauea Iki lava lake. Hawaii. Geochimica et Cosmochimica Acta 210, 71–96.

Gutiérrez, F., Parada, M.A., 2010. Numerical modeling of time-dependent fluid dynamics and differentiation of a shallow basaltic magma chamber. J. Petrol. 51, 731–762.

Haag, V., Houghton, B.F., Perugini, D., Soldati, A., 2024. Brittle fragmentation of Fissure 17 enclave magma revealed by fractal analysis. J. Volcanol. Geotherm. Res. 108087.

Helz, R. T., & Wright, T. L. (1992). Differentiation and magma mixing on Kilauea's east rift zone: a further look at the eruptions of 1955 and 1960. Part I. The late 1955 lavas. *Bulletin of Volcanology*, *54*, 361-384.

Helz, R.T., Thornber, C.R., 1987. Geothermometry of Kīlauea Iki lava lake. Hawaii. Bull. Volcanol. 49 (5), 651–668.

Ho, Ritchie A., Michael, O., 1988. Garcia. Origin of differentiated lavas at Kilauea Volcano, Hawaii: implications from the 1955 eruption. Bull. Volcanol. 50, 35–46.

Houghton, B.F., Tisdale, C.M., 2022, December. Complex Styles of Basaltic Explosive Volcanism from Fissure 17 of the 2018 lower East Rift Zone Eruption of Kilauea. AGU Fall Meeting Abstracts (Vol. 2022, pp. V51A-02).

Iacovino, K., Till, C.B., 2019. DensityX: A program for calculating the densities of magmatic liquids up to 1,627 C and 30 kbar. Volcanica 2 (1), 1–10.

Jones, T.J., Llewellin, E.W., 2021. Convective tipping point initiates localization of basaltic fissure eruptions. Earth and Planetary Science Letters 553, 116637.

Morimoto, N., 1988. Nomenclature of pyroxenes. Mineral. Petrol. 39 (1), 55–76.

Neal, C.A., Brantley, S.R., Antolik, L., Babb, J.L., Burgess, M., Calles, K., Damby, D., 2019. The 2018 rift eruption and summit collapse of Kīlauea Volcano. Science 363 (6425), 367–374.

Parfitt, E.A., Wilson, L., 1995. Explosive volcanic eruptions—IX. The transition between Hawaiian-style lava fountaining and Strombolian explosive activity. Geophys. J. Int. 121 (1), 226–232.

Pedersen, G.B.M., Höskuldsson, A., Dürig, T., Thordarson, T., Jonsdottir, I., Riishuus, M. S., Schmith, J., 2017. Lava field evolution and emplacement dynamics of the 2014–2015 basaltic fissure eruption at Holuhraun, Iceland. J. Volcanol. Geotherm. Res. 340, 155–169.

Pedersen, G.B., Belart, J.M., Óskarsson, B.V., Gudmundsson, M.T., Gies, N., Högnadóttir, T., Oddsson, B., 2022. Volume, effusion rate, and lava transport during the 2021 Fagradalsfjall eruption: results from near real-time photogrammetric monitoring. Geophys. Res. Lett. 49 (13) e2021GL097125.

Pietruszka, A.J., Garcia, M.O., Rhodes, J.M., 2021. Accumulated Pu'u ʻŌʻō magma fed the voluminous 2018 rift eruption of Kīlauea Volcano: evidence from lava chemistry. Bull. Volcanol. 83 (9), 1–18.

Putirka, K., Johnson, M., Kinzler, R., Longhi, J., Walker, D., 1996. Thermobarometry of mafic igneous rocks based on clinopyroxene-liquid equilibria, 0–30 kbar. Contrib. Mineral. Petrol. 123 (1), 92–108.

Schindelin, J., Arganda-Carreras, I., Frise, E., Kaynig, V., Longair, M., Pietzsch, T., Cardona, A., 2012. Fiji: an open-source platform for biological-image analysis. Nat. Methods 9 (7), 676–682. https://doi.org/10.1038/nmeth.2019.

Schmidt, M.W., Weidendorfer, D., 2018. Carbonatites in oceanic hotspots. Geology 46 (5), 435–438.
Soldati, A., Houghton, B.F., Dingwell, D.B., 2021. A lower bound on the rheological evolution of magmatic liquids during the 2018 Kīlauea eruption. Chem. Geol. 576, 120272.
Spina, La, Giuseppe, Fabio Arzilli, Llewellin, Edward W., Burton, Mike R., Amanda, B., Clarke, M., Vitturi, De Michieli, Polacci, Margherita, Hartley, Margaret E., Di Genova, Danilo, Mader, Heidy M., 2021. Explosivity of basaltic lava fountains is controlled by magma rheology, ascent rate and outgassing. Earth Planet. Sci. Lett. 553, 116658.
Thornber, C.R., 2001. Olivine–liquid relations of lava erupted by Kīlauea volcano from 1994 to 1998: implications for shallow magmatic processes associated with the ongoing East-Rift-Zone eruption. Can. Mineral. 39 (2), 239–266.
Thornber, C.R., Heliker, C., Sherrod, D.R., Kauahikaua, J.P., Miklius, A., Okubo, P.G., Meeker, G.P., 2003. Kīlauea east rift zone magmatism: An episode 54 perspective. J. Petrol. 44 (9), 1525–1559.
Thornber, C.R., Orr, T.R., Heliker, C., Hoblitt, R.P., 2015. Petrologic testament to changes in shallow magma storage and transport during 30+ years of recharge and eruption at Kīlauea Volcano, Hawai ʻi. Hawaiian Volcanoes: From Source Surf. 208, 147–188.
Walker, Brett Halsey, Houghton, Bruce F., Llewellin, Edward W., 2023. Coexisting Strombolian and Hawaiian activity during the 2018 fissure eruption of Kīlauea–Implications for processes of weak explosions. J. Volcanol. Geotherm. Res. 435, 107754.
Waters, L.E., Lange, R.A., 2015. An updated calibration of the plagioclase-liquid hygrometer-thermometer applicable to basalts through rhyolites. Am. Mineral. 100 (10), 2172–2184.
Weidendorfer, D., Schmidt, M.W., Mattsson, H.B., 2019. Mineral resorption triggers explosive mixed silicate–carbonatite eruptions. Earth Planet. Sci. Lett. 510, 219–230.
Wieser, P.E., Edmonds, M., Gansecki, C., Maclennan, J., Jenner, F.E., Kunz, B., Antoshechkina, P., Trusdell, F., Lee, R.L., 2022. Explosive activity on Kīlauea's lower East Rift Zone Fueled by a Volatile-Rich, Dacitic Melt. Geochem. Geophys. Geosyst. 23 (2) e2021GC010046.
Wright, T. L. (1971). *Chemistry of Kilauea and Mauna Loa lava in space and time* (No. 735). US Govt. Print. Off.,.
Wright, T.L., Fiske, R.S., 1971. Origin of the differentiated and hybrid lavas of Kilauea volcano, Hawaii. Journal of Petrology 12 (1), 1–65.